ORIGINAL PAPER

The effect of initial H_2O concentration on decompression-induced phase separation and degassing of hydrous phonolitic melt

A. Allabar[1] · E. Salis Gross[1] · M. Nowak[1]

Abstract

Supersaturation of H_2O during magma ascent leads to degassing of melt by formation and growth of vesicles that may power explosive volcanic eruptions. Here, we present experiments to study the effect of initially dissolved H_2O concentration (c_{H2Oini}) on vesicle formation, growth, and coalescence in phonolitic melt. Vesuvius phonolitic melts with c_{H2Oini} ranging between 3.3 and 6.3 wt% were decompressed at rates of 1.7 and 0.17 MPa·s^{-1} and at temperatures $\geq$ 1323 K. Decompression started from 270 and 200 MPa to final pressures of 150–20 MPa, where samples were quenched isobarically. Optical microscopy and Raman spectroscopic measurements confirm that the glasses obtained were free of microcrystals and Fe-oxide nanolites, implying that the experiments were superliquidus and phase separation of the hydrous melt was homogeneous. A minimum number of the initially formed vesicles, defined by the number density normalized to vesicle-free glass volume (VND), is observed at ~ 5 wt% c_{H2Oini} with a logVND of ~ 5 (in mm^{-3}). The logVND increases strongly towards lower and higher c_{H2Oini} by one order of magnitude. Furthermore, an important transition in evolution of vesiculation occurs at ~ 5.6 wt% c_{H2Oini}. At lower c_{H2Oini}, the initial VND is preserved during further decompression up to melt porosities of 30–50%. At higher c_{H2Oini}, the initial vesicle population is erased at low melt porosities of 15–21% during further decompression. This observation is attributed to vesicle coalescence favored by low melt viscosity. In conclusion, c_{H2Oini} determines the VND of initial phase separation and the evolution of vesiculation during decompression that controls the style of volcanic eruptions.

Keywords Vesicle number density · Phonolitic melt · Spinodal decomposition · Melt degassing · H_2O concentration · Fe-oxide nanolites

Introduction

Explosive volcanic activity is powered by rapid melt degassing of mainly H_2O, prior to and during fragmentation (e.g., Alidibirov and Dingwell 1996; Gonnermann and Manga 2007). Supersaturation of hydrous silicate melt induced e.g., by decompression drives vesicle formation and growth (e.g., Sparks 1978; Hurwitz and Navon 1994; Mourtada-Bonnefoi and Laporte 2004; Iacono-Marziano et al. 2007; Hamada et al. 2010; Gardner and Ketcham 2011; Preuss et al. 2016; Shea 2017; Hajimirza et al. 2019). The number of vesicles per unit volume of melt (VND), and thus the inter-vesicle distance, defines the degassing efficiency (e.g., Toramaru 2006; Allabar and Nowak 2018). The coupled magma density decrease amplifies ascent, volatile expansion, and fragmentation, and powers explosive volcanic eruptions (e.g., Kueppers et al. 2006; Genareau et al. 2012).

According to nucleation theory, which describes phase separation in the thermodynamically metastable state, the VND increases strongly with the decompression rate dP/dt (e.g., Hurwitz and Navon 1994; Toramaru 2006). In contrast to this dependence, a decompression rate independent VND was reported by Allabar and Nowak (2018) for hydrous phonolitic melt with white pumice composition of the Vesuvius 79AD eruption (VAD79). This composition is representative for other natural phonolitic and trachytic volcanic systems like the Campi Flegrei or Tambora that are known for violent explosive eruptions (e.g., Mastrolorenzo et al. 2001; Foden

✉ A. Allabar
anja.allabar@uni-tuebingen.de

1   Department of Geosciences, University of Tübingen, Wilhelmstraße 56, 72074 Tübingen, Germany

1986). The observed independence of *VND* on decompression rate in the investigated range of 0.024–10 MPa·s^{-1} is inconsistent with the theory of vesicle nucleation as phase separation mechanism. Alternatively, phase separation may be described by the theory of spinodal decomposition in the thermodynamically unstable state, for which the *VND* is expected to be independent from decompression rate (Allabar and Nowak 2018). Their experimentally observed log*VND*s (in mm^{-3}) of ~5.2 at initial H_2O concentration (c_{H2Oini}) of ~5.3 wt% match the lower end of the range of log*VND* of 5.15–7.08 recorded in natural VAD79 pumice (Gurioli et al. 2005; Shea et al. 2010a). However, natural eruptive products of the different stages of the AD79 Vesuvius eruption have been reported to originate from melts with c_{H2Oini} ranging between 3.0 and 6.4 wt% (Cioni 2000). So far, degassing of superliquidus phonolitic melt by homogeneous phase separation has been investigated as a function of decompression rate (Iacono-Marziano et al. 2007; Marxer et al. 2015; Preuss et al. 2016; Allabar and Nowak 2018) and slight variations in decompression temperature (1323–1373 K; Allabar and Nowak 2018). A systematic investigation of the effect of c_{H2Oini} on homogeneous phase separation of phonolitic melt during decompression is lacking. Dissolved H_2O significantly influences physicochemical parameters of silicate melt such as viscosity (e.g., Giordano et al. 2008), H_2O diffusivity (e.g., Nowak and Behrens 1997; Fanara et al. 2013), and surface tension (e.g., Bagdassarov et al. 2000). It is thus expected that c_{H2Oini} of silicate melt controls homogeneous phase separation by vesicle formation and the evolution of vesiculation during decompression. Therefore, experimental data of decompressed hydrous phonolitic VAD79 melt are compiled that fulfill the experimental protocol of Preuss et al. (2016) ensuring homogeneous phase separation (Iacono-Marziano 2007; Marxer et al. 2015; Preuss et al. 2016; Allabar and Nowak 2018). These data are extended by additional decompression experiments at temperatures (*T*) between 1323 and 1523 K using VAD79 melt with varying c_{H2Oini} ranging between 3.3 and 6.3 wt% and a d*P*/d*t* of 0.17 MPa·s^{-1}.

Experimental methods

Starting material

Crystal-free homogeneous starting glasses of the VAD79 white pumice composition (Iacono-Marziano et al. 2007) were synthesized following the procedure of Marxer et al. (2015) in combination with the cooling optimization described by Allabar and Nowak (2018). Analytical-grade oxide (SiO$_2$-glass, TiO$_2$, Al$_2$O$_3$, FeO, MgO, MnO) and carbonate (CaCO$_3$, Na$_2$CO$_3$, K$_2$CO$_3$) powders as well as (NH$_4$)$_2$HPO$_4$ as phosphorous source were used as raw

materials for glass synthesis. To obtain accurate weight portions, the strongly hygroscopic SiO_2, Al_2O_3, and MgO powders were dried at 1073 K for 18 h, and the carbonate powders were dried at 383 K for 24 h and, subsequently, cooled and stored in a desiccator. The dried powders were weighed to obtain 50 g of glass for each batch. The powders were ground and mixed in a ZrO_2 ball mill for homogenization. One powder mixture used for the glass batch (VAD79_12) was ground in a corundum ball mill to minimize possible ZrO_2 contamination. Enrichment of ZrO_2 may lead to nanometer-sized Zr phases (Cormier et al. 2015; Dargaud et al. 2011) prior or during decompression of hydrous melt. Crystalline phases even at a nanometer scale may initiate heterogeneous H_2O vesicle nucleation (e.g., Shea 2017) that has to be avoided to study homogeneous phase separation.

The powder mixtures were decarbonated and fused in a Pt90Rh10 crucible by heating to 1873 K. After 6 h heating, the melts were rapidly quenched in deionized water. The cracked glasses were crushed and ground in the respective ball mills and melted again for 1 h at 1873 K. To inhibit crystallization, the melts were then air-cooled within 1–2 min close to the glass transition temperature (T_g) of 937 K, calculated after Giordano et al. (2008) assuming an H_2O content of 1000 ppm. Subsequently, the supercooled melts were transferred into a furnace preheated to 833 K. The furnace was then switched off to maintain a cooling rate of ~5 K·min^{-1}. This cooling procedure was fast enough to inhibit partial crystallization, and stress-induced cracking within the glass batches was minimized when cooling to room temperature. The compositions of the VAD79 glasses measured prior to the decompression experiments are given in Table 1.

Cylinders with a diameter of 5 mm were drilled from the glass batches and cut to lengths of 5.3–6.7 mm. The sharp cylinder edges were rounded with abrasive paper to prevent capsule damage during pressurization. The porosity of the glass cylinders, caused by some air vesicles trapped during melt synthesis, was determined by pycnometry to confirm porosities < 6% prior to the combined hydration and decompression experiments (Preuss et al. 2016).

Capsule preparation

A sufficiently large capsule volume has to be ensured, which is capable of containing the melt with equilibrium porosity (Φ_{equ}) without bursting during decompression to the relevant final pressure (P_{final}). Therefore, the Φ_{equ} at each P_{final} was calculated using the expected porosity equation of Gardner (1999) (Eq. 5 therein). The H_2O solubility dependence from solubility experiments of Iacono-Marziano et al. (2007) and Marxer et al. (2015), the equation of state (EOS) for H_2O of Duan and Zhang (2006), and the melt density calculation of Ochs and Lange (1999) were used for calculation.

Table 1 Bulk glass compositions (in wt%) of synthesized VAD79 glasses, used for decompression experiments based on white pumice composition given in Iacono-Marziano (2007) (VAD79[IM07]) and measured by electron microprobe analysis after glass synthesis and normalized to 100%

	VAD79[IM07]	VAD79_03	VAD79_06	VAD79_07	VAD79_08	VAD79_10	VAD79_12[♯]
SiO_2	57.15 (39)	57.66 (43)	56.97 (44)	57.19 (56)	57.82 (27)	57.40 (39)	57.73 (34)
TiO_2	0.30 (05)	0.29 (03)	0.30 (02)	0.29 (02)	0.28 (02)	0.29 (02)	0.28 (03)
Al_2O_3	21.34 (25)	20.96 (31)	21.27 (19)	21.15 (19)	20.69 (23)	20.77 (24)	20.77 (34)
FeO	2.70 (17)	2.70 (18)	2.74 (17)	2.72 (21)	2.69 (11)	2.72 (05)	2.62 (11)
MnO	0.14 (06)	0.14 (03)	0.16 (03)	0.15 (04)	0.14 (04)	0.14 (02)	0.14 (03)
MgO	0.39 (05)	0.39 (03)	0.39 (03)	0.36 (04)	0.38 (04)	0.37 (04)	0.30 (02)
CaO	3.26 (12)	3.2 (18)	3.27 (10)	3.15 (10)	3.10 (09)	3.19 (08)	3.17 (10)
Na_2O	5.16 (15)	5.38 (18)	5.31 (20)	5.37 (18)	5.37 (19)	5.40 (20)	5.32 (17)
K_2O	9.46 (15)	9.17 (57)	9.52 (16)	9.41 (12)	9.39 (14)	9.62 (16)	9.49 (23)
P_2O_5	0.09 (04)	0.10 (03)	0.08 (03)	0.09 (03)	0.09 (03)	0.10 (07)	0.08 (03)
ZrO_2	n.d.	n.d.	n.d.	0.12 (05)	0.10 (05)	n.d.	0.06 (02)

ZrO_2 concentrations are mean of measured concentrations above detection limit of ~350 ppm

n.d.: ZrO_2 was not determined in these glasses

Numbers in brackets are 1σ standard deviations

♯Synthesized using a corundum ball mill; all other batched were synthesized using a ZrO_2 ball mill

The resulting sample volumes were considered for the relationship of capsule to glass cylinder length. Cleaned and annealed Au80Pd20 tubes (13 mm length, 5 mm inner diameter) were closed with an electric arc-welded lid at the bottom. Glass cylinders were inserted into the capsules together with the desired amount of water. The top of each capsule was crimped to a three-sided star and welded shut while cooling with liquid nitrogen to prevent H_2O loss by vaporization. A typical weight loss by welding-induced capsule metal loss is ~0.3 mg for the used design. If the weight loss of glass and water filled capsules m_{wl} was determined to be > 0.3 mg after welding, m_{wl}-0.3 mg was attributed to H_2O loss as expressed in the negative errors given in Table 2 for the gravimetrically determined initial H_2O concentration ($c_{H2Ograv}$). However, it may be possible that more than 0.3 mg Au80Pd20 is lost instead of H_2O during welding. This would result in an overestimation of the negative error of $c_{H2Ograv}$. To check for possible leakage, the capsules were stored in a compartment dryer at 383 K, pressurized to 100 MPa at ambient T in a cold seal pressure vessel and again stored in a compartment dryer. After each step, the weight of the capsule was checked to exclude leakage prior to the decompression experiments.

Decompression experiments

Experimental technique

The combined hydration and decompression experiments were performed in an internally heated argon pressure vessel (IHPV) equipped with a rapid quench setup and a piezo-actuator driven high-pressure valve for continuous decompression (Berndt et al. 2002; Nowak et al. 2011). The intrinsic redox condition of the IHPV is 3.5 log units above the

quartz fayalite magnetite (QFM) buffer at H_2O saturated run conditions (Berndt et al. 2002). All samples were hydrated for at least 94 h at T ranging between 1500 and 1550 K at a starting pressure (P_{start}) of 200 MPa, except of CD83 and the samples with c_{H2Oini} > 5.6 wt%, which were hydrated at 198 and 270 MPa, respectively. After hydration, T was decreased to superliquidus decompression temperatures (T_d) ranging between 1323 and 1523 K (Table 2) and thermally equilibrated for at least 0.5 h before isothermal decompression was initiated. Two control thermocouples recorded sample temperature gradients of < 20 K over a distance of ~12 mm. Because the sample length is lower (< 6.7 mm) than the distance of the two thermocouples, the T gradient within the samples is < 10 K.

For the decompression rates ≥ 0.17 MPa·s⁻¹, the micrometer screw of the decompression valve was used to release pressure manually. During decompression, T decreased by ~5–10 K due to adiabatic cooling that could not fully be compensated by the digitally controlled furnace power. Only during decompression of sample CD95, which was decompressed to the lowest P_{final} of 20 MPa, the maximum T drop was ~50 K at P_{final}. At P_{final}, the decompression valve was closed and the capsules were isobarically quenched using an electrical power supply to melt the quench platinum wire, at which the capsules were suspended in the sample holder. Successful capsule drop was confirmed by a monitored T decrease ranging between 2 and 10 K in the hot zone of the furnace. The maximum achievable cooling rate of the IHPV is about 150 K·s⁻¹ (Berndt et al. 2002). However, this cooling rate induces stress-induced cracks within the quenched glass samples. This leads to disintegration of the samples during further preparation. Therefore, a 35 mm brass cylinder was mounted at the bottom of the sample holder to reduce the cooling rate and thus crack formation during

Table 2 Experimental conditions and results. All samples were hydrated prior to decompression for at least 94 h at 1500–1550 K at P_{start}. The c_{H2Oini} printed in bold numbers are the c_{H2Oini} of the experiments

Series	Sample	Glass batch VAD79_	Vesicle population	P_{start} [MPa]	P_{sat} [MPa]	T_d [K]	P_{final} [MPa]	dP/dt [MPa·s⁻¹]	t_d [min]	$c_{H2Ograv}$ [wt%]	+	−	c_{H2OIR} [wt%]	Φ_{glass} [vol%]	VND [mm⁻³]	logVND [mm⁻³]	References
No vesicles observed																	
C	RefA_2	10	–	200	192	1323	–	–	–	5.27	0.10	0.10	5.26±0.05	–	–	–	–
C	CD93	12	–	200	88	1323	60	0.17	2.7	3.34	0.10	0.10	3.28±0.03	–	–	–	–
C	CD86	10	–	200	147	1323	80	0.17	6.5	4.35	0.11	0.23	4.47±0.03	–	–	–	–
C	CD48	7	–	200	199	1323	110	0.17	8.7	5.32	0.09	0.09	5.37±0.06	–	–	–	AN18
Vesiculated samples																	
C	CD94	12	Main	200	94	1323	40	0.17	5.3	3.40	0.10	0.10	**3.43±0.05**	0.3±0.1	9.11E+05^a	5.96	
C	CD95	12	Main	200	91	1323	20	0.17	7.0	**3.36**	**0.12**	**0.12**	–	15.4±2.1	2.35E+06^b	6.37	
C	CD87	10	Main	200	138	1323	60	0.17	7.7	**4.31**	**0.10**	**0.10**	–	5.4±1.3	3.26E+05^ab	5.51	
			Second (cap)											0.3±0.1	5.23E+05^a	5.72	
C	CD85	10	Main	200	138	1323	40	0.17	9.6	**4.30**	**0.13**	**0.34**	–	24.4±2.2	2.83E+05^b	5.45	
			Second (cap)										4.27±0.07	3.2±0.5	1.38E+06^c	6.14	
			Second (ves)										4.27±0.07	0.2±0.1	4.61E+05^a	5.66	
C	CD-C-23	3	Main	200	167	1323	100	0.17	6.6	4.76	0.10	0.10	**4.83±0.06**	<0.1	1.01E+05^a	5.00	PR16
C	CD40	8	Main	200	187	1323	100	0.17	8.5	5.27	0.09	0.09	**5.17±0.09**	<0.1	1.40E+05^a	5.15	AN18
C	CD42	8	Main	200	189	1323	90	0.17	9.7	5.31	0.09	0.09	**5.20±0.09**	1.1±0.1	9.59E+04^b	4.98	
C	CD63	7	Main	200	195	1323	80	0.17	11.2	**5.30**	**0.10**	**0.10**	–	7.0±0.7	1.74E+05^b	5.24	AN18
C	CD39	8	Main	200	175	1323	80	0.17	9.3	5.34	0.09	0.09	**4.97±0.13**	4.5±0.5	1.49E+05^b	5.17	AN18
C	CD91	12	Main	200	197	1323	80	0.17	11.4	**5.33**	**0.10**	**0.10**	–	9.0±1.1	2.56E+05^bc	5.41	AN18
			Second (cap)										5.20±0.13	1.3±0.4	9.26E+05^a	5.97	
C	CD83	12	Main	198	198	1323	80	0.17	11.6	5.34*	0.17	0.17	**5.46±0.07**	3.2±1.0	6.08E+05^a	5.78	
C	CD50	7	Main	200	195	1323	70	0.17	12.2	**5.30**	**0.09**	**0.09**	–	13.1±1.4	6.70E+04^ab	4.83	AN18
C	CD73	10	Main	200	200	1323	60	0.17	13.7	**5.46***	**0.17**	**0.17**	–	18.5±2.2	3.03E+05^bc	5.41	
			Second (cap)										4.99±0.18	1.0±0.3	8.14E+05^a	5.91	
			Second (cap)										–	9.0±1.0	1.16E+06^c	6.07	
C	CD102	12	Main	270	255	1323	150	0.17	10.3	6.30	0.10	0.41	**6.24±0.03**	0.2±0.1	4.99E+05^a	5.70	
C	CD101	12	Main	270	258	1323	145	0.17	11.1	6.30	0.11	0.29	**6.28±0.11**	2.3±0.7	6.08E+05^ac	5.78	
C	CD97	12	Coalesced	270	260	1323	120	0.17	13.7	**6.30**	**0.09**	**0.15**	–	8.9±1.4	8.27E+01^b	1.92	
C	CD98	12	Main	270	237	1323	140	0.17	9.5	6.27	0.10	0.47	**5.96±0.06**	0.3±0.1	6.85E+05^a	5.84	
C	CD100	12	Main (clouds)	270	224	1323	100	0.17	12.2	**5.77**	**0.10**	**0.17**	5.43±0.07	0.2±0.1	8.08E+05^a	5.91	
			Coalesced										–	9.3±2.3	5.54E+01^b	1.74	

Table 2 (continued)

Series	Sample	Glass batch VAD79_	Vesicle population	P_{start} [MPa]	P_{sat} [MPa]	T_d [K]	P_{final} [MPa]	dP/dt [MPa•s^{-1}]	t_d [min]	$c_{H2Ograv}$ [wt%]	+	−	c_{H2OIR} [wt%]	Φ_{glass} [vol%]	VND [mm^{-3}]	logVND [mm^{-3}]	References
D	CD92	10	Main	200	183	1323	80	0.064	26.7	5.27	0.10	0.10	**5.10 ± 0.09**	4.6 ± 0.6	2.25E+05[b]	5.35	AN18
D	CD78	10	Main	200	184	1323	82	1.7	1.0	5.30	0.11	0.11	**5.12 ± 0.05**	3.3 ± 0.6	2.11E+05[ab]	5.32	AN18
D	B74	–	Main	200	200	1323	70	1.69	1.3	**5.46***	**0.16**	**0.16**	5.09#± 0.5	5.0 ± 1.0	5.65E+05	5.75	IM07
D	B72	–	Main	200	200	1323	75	4.63	0.4	**5.46***	**0.16**	**0.16**	5.22#± 0.35	6.0 ± 1.0	7.71E+05	5.89	IM07
D	SSD06	2	Main	200	200	1323	75	10	0.2	**5.46***	**0.16**	**0.16**	–	15.0 ± 1.5	2.57E+05[b]	5.41	MA15
D	CD28	3	Main	200	194	1323	95	1.7	1.0	5.34	0.10	0.10	**5.29 ± 0.06**	0.5 ± 0.1	1.12E+05[ab]	5.05	
D	CD-C-25	3	Main	200	158	1323	100	0.024	40.5	4.66	0.10	0.10	**4.68 ± 0.05**	<0.1	1.30E+05[a]	5.11	PR16
D	CD77	10	Main	200	160	1323	80	0.024	55.6	5.29	0.11	0.17	**4.71$ ± 0.03**	<0.1	2.45E+05[a]	5.39	AN18
TD	CD59	6	Main	200	189	1373	110	1.7	0.8	5.44	0.10	0.10	**5.21 ± 0.05**	<0.1	3.02E+05[a]	5.48	
TD	CD55	6	Main	200	190	1373	100	1.7	0.9	5.29	0.10	0.10	**5.22 ± 0.05**	0.5 ± 0.1	3.96E+04[ab]	4.60	
TD	CD57	6	Main	200	196	1373	100	1.7	0.9	5.32	0.10	0.10	**5.32 ± 0.07**	<0.1	6.02E+04[a]	4.78	
TD	CD51	7	Main	200	193	1373	75	1.7	1.2	5.33	0.09	0.17	**5.27 ± 0.11**	4.2 ± 0.9	9.58E+04[ab]	4.98	AN18
T	CD52	7	Main	200	189	1373	90	0.17	9.7	5.33	0.10	0.10	**5.21 ± 0.07**	1.6 ± 0.4	9.18E+04[ab]	4.96	
T	CD53	7	Main	200	187	1373	80	0.17	10.5	5.28	0.10	0.10	**5.17 ± 0.06**	1.5 ± 0.2	9.00E+04[b]	4.95	AN18
T	CD44	8	Half capsule	200	174	1523	80	0.17	9.3	5.28	0.10	0.10	**4.96$ ± 0.18**	<0.1	7.37E+05[a]	5.87	

P_{start} hydration pressure and starting pressure of decompression, P_{sat} saturation P calculated from dependency of H_2O solubility experiments by Iacono-Marziano et al. (2007) and Marxer et al. (2015), for supersaturated experiments $P_{start} = P_{sat}$, T_d = decompression temperature, P_{final} final pressure, at which samples were isobarically quenched, dP/dt decompression rate, t_d decompression time = $(P_{sat} - P_{final})/(dP/dt)$, $c_{H2Ograv}$ gravimetrically determined H_2O concentration in the capsule, c_{H2OIR} total H_2O concentration measured by FTIR with vesicles in beam, Φ_{glass} glass porosity, VND vesicle number density normalized to vesicle-free glass, analyzed with: [a]transmitted light microscopy, [b]SEM-BSE-imaging, [c]laser scanning microscopy imaging, (ves) in the drainage zone of a large vesicle, (cap) in drainage zone towards the capsule wall

*Supersaturated conditions; value corresponds to solubility at hydration P and T_d

$Diffusional H_2O loss towards fringe vesicles prior to phase separation due to low decompression rate (Allabar and Nowak 2018)

$Diffusional H_2O loss prior to phase separation due to high diffusivity at high T_d

#EMPA by-difference method between vesicles (Devine et al. 1995)

References PR16: Preuss et al. (2016); AN18: Allabar and Nowak (2018); IM07: Iacono-Marziano et al. (2007); MA15: Marxer et al. (2015)

quench. The medium quench rate (MQ) of 44 ± 11 K·s^{-1} (Allabar et al. 2020) inhibited disintegration of the samples during preparation.

Experimental decompression conditions

The data for published decompression experiments using VAD79 white pumice composition (Iacono-Marziano et al. 2007; Marxer et al. 2015; Preuss et al. 2016; Allabar and Nowak 2018) that fulfill the experimental protocol given in Preuss et al. (2016) are compiled in Table 2. The experimental protocol ensures homogeneous phase separation by vesicle formation in the central part of the sample without effects of the experimental design or capsule size. Therefore, only data of experiments using glass cylinders were considered to exclude *VND* data influenced by pre-existing vesicles induced by the use of glass powder as starting material (Preuss et al. 2016). Additionally, the limitation of decompression rate defined by the sample diameter is considered, ensuring a central sample volume that is unaffected by diffusional H_2O loss into early-formed fringe vesicles at the capsule wall and by vesicles ascending from the capsule bottom into the central melt volume (Iacono-Marziano et al. 2007; Marxer et al. 2015; Preuss et al. 2016; Allabar and Nowak 2018). At a decompression rate of 0.024 MPa·s^{-1}, homogeneous phase separation is facilitated only in a small central melt volume that is already affected by diffusional H_2O loss into fringe vesicles using 5 mm diameter samples with 5.3 wt% c_{H2Oini} (Allabar and Nowak 2018). This defines the decompression rate limit for capsules with 5 mm diameter at the given H_2O concentration. With decreasing c_{H2Oini}, the H_2O diffusivity and, consequently, the H_2O-depleted drainage zone width decrease. This expands the feasible decompression rate towards lower values, at which homogeneous phase separation can still be observed in the central sample volume.

The compiled published VAD79 superliquidus decompression experiments were extended during this study by additional experiments to obtain four experimental series and an un-decompressed reference sample (Table 2): (1) To investigate the influence of c_{H2Oini} on the degassing behavior of phonolitic melt, the C-Series was performed with fixed T of 1323 K and a dP/dt of 0.17 MPa·s^{-1}, while the c_{H2Oini} was changed. Therefore, the experimental set given in Allabar and Nowak (2018) with a c_{H2Oini} of 5.3 wt% H_2O was extended by experiments with higher (~ 6.3 wt%) and lower c_{H2Oini} (~ 3.3 and ~ 4.3 wt%; Table 2; Fig. 1). These samples were decompressed to P_{final} ranging between 20 and 150 MPa. The 5.3 wt% c_{H2Oini} data set of Allabar and Nowak (2018) at a dP/dt of 0.17 MPa·s^{-1} was extended by an experiment with a P_{final} of 60 MPa (CD73). The sample CD83 was hydrated with excess H_2O to prove that there is no difference in *VND* after decompression from H_2O supersaturated
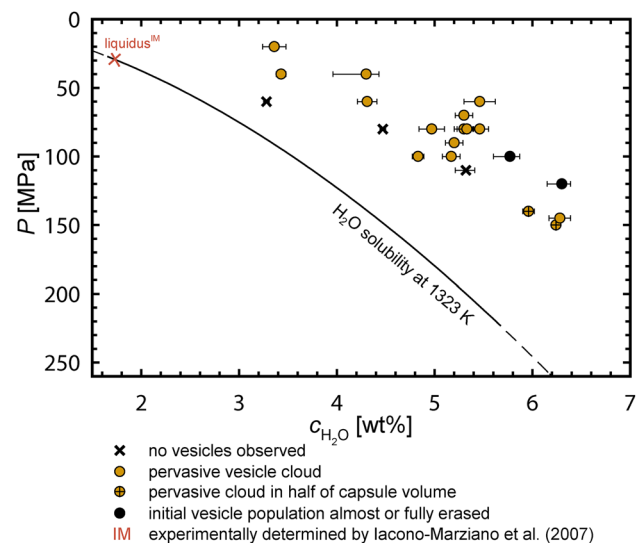
Fig. 1 Experiments of the C-Series plotted at final pressure (P_{final}) and initial H_2O concentration (c_{H2Oini}) (Table 2). Symbol fillings indicate textural features of the samples. The samples were decompressed with 0.17 MPa·s^{-1} at 1323 K and quenched with 44 K·s^{-1} (MQ). The H_2O solubility curve (solid line) is derived from solubility experiments of Iacono-Marziano et al. (2007) and Marxer et al. (2015) (c_{H2O} [wt%] $= 0.2321 \cdot P$[MPa]$^{0.5928}$) and extrapolated towards high c_{H2O} (dashed end of line). The cross with the index "liquidus^{IM}" marks the P with corresponding equilibrium c_{H2O} at which the liquidus was experimentally determined (Iacono-Marziano et al. 2007; Marxer et al. 2015). Pervasive vesicle clouds within the central sample volumes are observed in all vesiculated samples with $c_{H2Oini} < 5.6$ wt%. These clouds are stable down to low P_{final}. At higher c_{H2Oini}, the initially formed main vesicle population is erased at relatively high P_{final} of ≥ 100 MPa

(CD73 of this study and experiments by Iacono-Marziano et al. 2007 and Marxer et al. 2015) and H_2O undersaturated conditions (Preuss et al. 2016, Allabar and Nowak 2018, this study). To obtain a similar c_{H2Oini}, CD83 was hydrated at 198 MPa, where H_2O solubility is 5.34 wt% (Iacono-Marziano et al. 2007; Marxer et al. 2015). In this case, the homogenization time after T decrease from hydration T to T_d was 1.5 h to ensure re-equilibration and homogenization of H_2O concentration due to increasing solubility with decreasing T (Schmidt and Behrens 2008). The experiment CD-C-23 of Preuss et al. (2016) also fulfills the experimental parameters of the C-Series. (2) Experiments of the D-Series were performed with a c_{H2Oini} of ~ 5.3 wt%. This series is a compilation of experiments performed at 1323 K with variable decompression rates. The experiments from Allabar and Nowak (2018), and experiments listed therein, were extended by the experiment CD28 decompressed with 1.7 MPa·s^{-1}. (3) To ensure T_d being well above the liquidus, experiments at 1373 K were performed (Allabar and Nowak 2018) at decompression rates of 1.7 MPa·s^{-1} (TD-Series)

and (4) 0.17 MPa·s^{-1} (T-Series). The experiment CD44 was decompressed at 1523 K with the latter rate.

The sample Ref_A2 was hydrated with 5.3 wt% H_2O at 1523 K and 200 MPa. The sample was quenched with MQ without decompression after the T decrease to 1323 K and a homogenization time of 0.5 h. Therefore, this sample represents the initial state of the samples with c_{H2Oini} of 5.3 wt% prior to decompression.

Sample preparation

Pieces from the starting glass batches were embedded in epoxy resin and ground and polished for electron microprobe analysis (EMPA). The decompressed samples and the hydrated sample REF_A2 were cut along the cylinder axis. One half was embedded in epoxy resin and ground and polished for EMPA, scanning electron microscopy (SEM), laser scanning microscopy (LSM), and Raman micro-spectroscopy (RMS). The other halves were unwrapped from the capsule material, embedded with epoxy resin in glass–ceramic rings, and ground to a thickness of 100–320 μm. These samples were polished on both sides to obtain thin sections for Fourier transform infrared micro-spectroscopy (FTIR) and transmitted light microscopy analysis (TLM). Sample thickness was measured with a Mitutoyo digital micrometer (± 3 μm).

Analytical methods

Electron microprobe analysis

After glass synthesis, pieces of each glass batch were analyzed with a JEOL JXA 8900 R electron microprobe to confirm chemical composition and homogeneity (Table 1). EMPA WDS measurements were conducted with an acceleration voltage of 15 kV, 3 nA beam current, and a defocused beam of 20 μm to optimize for Na analysis (Devine et al. 1995). Peak counting times were set to 10 s (Na), 16 s (Si, Al, Fe, Mg, Ca, K), and 30 s (Ti, Mn, P) according to Preuss et al. (2016). Zr was additionally analyzed in glasses VAD79_07, 08, and 12 with a peak counting time of 60 s. 15–20 randomly distributed points were measured for each glass. The results (Table 1) agree within error with the VAD79 white pumice composition given in Iacono-Marziano et al. (2007).

Quantitative determination of *VND* and porosity

VND and glass porosity (Φ_{glass}) were determined in the central part of the samples where they are texturally homogeneous. Thus, convection-like patterns and effects of the capsule–melt contact, such as heterogeneously formed fringe vesicles and H_2O-depleted drainage zones, were excluded from quantitative analysis (see results for further textural features). Sample vesicle textures with average vesicle diameters of > 5 μm were analyzed with backscattered electron (BSE) or LSM images. *VND*s of samples containing smaller vesicles were quantified in thin sections with transmitted light microscopy. In some samples, several areas (BSE) and volumes (TLM) were analyzed (Table 2). Analysis of up to three areas within one sample resulted within error (± 0.13 log units, see description below) in similar *VND* and Φ_{glass}. Mean values are, therefore, given in Table 2.

Quantitative SEM and LSM image analysis

BSE images of the intersected samples were recorded with a LEO 1450 VP SEM or a Hitachi TM2020plus tabletop SEM, using individual magnifications of 150–2000× to resolve the smallest detectable vesicle intersections on a μm scale. Several adjacent images were recorded and stitched for analysis. Surfaces of the intersected samples were imaged with a Keyence VK-X100 confocal laser scanning microscope. These images with contrast-rich surface information were treated similarly as the BSE images for quantitative image analysis. Both methods yielded similar *VND* within error, as tested with the sample CD73 for reference. BSE or LSM images were quantitatively analyzed with ImageJ combined with a stereological 2D to 3D transformation, using CSDCorrections (Higgins 2000) as described in detail by Marxer et al. (2015) and Preuss et al. (2016). An analytical error in *VND* determination of ± 0.13 log units was estimated considering all steps that are prone to errors, such as the choice of different analyzed areas within a sample, different operators for counting vesicles, or filling of vesicle intersections by blackening, to obtain sufficient contrast between glass and intersected vesicles for image analysis. Errors in porosity from image analysis were provided by CSDCorrections.

Transmitted light microscopy

Vesicles were quantified in the thin sections by marking the vesicles, while focusing through the samples with a Zeiss Axio Image M2M microscope, using the Fission Track Studio software "Trackworks". The sizes of the analyzed areas were chosen individually for each measurement ranging between 2.3·10^{-2} and 8.5·10^{-5} mm^2. Together with the sample thickness, this defines the size of the analyzed volume used to normalize the counted number of vesicles to the number of vesicles per mm^3. Mean vesicle diameters were determined with the software-provided measurement tool to calculate Φ_{glass} and *VND*. Furthermore, inspection with TLM ensured microlite-free experimental samples. Errors from TLM analysis were calculated with an error propagation calculation using the error in sample thickness of ± 3 μm

and assuming an error of 10% for vesicle size measurement, and 5% for the vesicle count.

Raman micro-spectroscopy

RMS was used to detect possible Fe-oxide nanolitization of the glasses, which is suggested to significantly affect the degassing behavior of supersaturated hydrous melt (Di Genova et al. 2017a, 2018; Shea 2017). The hydrated samples REF02 (Marxer et al. 2015), Ref_A2 (this study), and the partly degassed samples CD73 and CD95 with VAD79 composition were measured for this purpose. For comparison, hydrated glasses (IB_C_1a, IB_P2), a nominally dry glass (CI_glass), and a partly degassed sample (CD_C_5) from Preuss et al. (2016) with trachytic Campanian Ignimbrite (CI) composition, which shows similar degassing behavior to VAD79 melt (Preuss et al. 2016), were analyzed. Raman spectra were collected using a Renishaw InVia confocal Raman micro-spectrometer equipped with a 532 nm laser, a 1800 grooves·mm^{-1} grating and an Peltier-cooled CCD detector. Laser power was set to 10%, which corresponds to a laser power of ~ 2.5 mW on the sample. This energy is sufficiently low to avoid oxidation (Di Genova et al. 2017a) and dehydration of the samples. A 50× objective with a numerical aperture of 0.75 was used together with the standard confocality setting. Focus depth was adjusted 6 μm below the sample surface to optimize the signal intensity (Di Genova et al. 2017a). Spectra were collected ranging between 300 and 950 cm^{-1}, and acquisition times were 10 s for each of three accumulations.

FTIR micro-spectroscopy

Near-infrared (NIR) measurements were performed with a Hyperion 3000 IR microscope connected to a Bruker Vertex v80 FTIR spectrometer to determine total H_2O contents (c_{H2OIR}) of the decompressed samples. A tungsten light source, a CaF_2 beam splitter, and an InSb single-element detector were used together with a 15× Cassegrain objective. For each measurement, 50 scans in transmission mode were recorded with a spectral resolution of 4 cm^{-1} using air as reference. Following the method of Behrens et al. (1996), the total H_2O contents were determined from molecular H_2O (~ 5210 cm^{-1}) and hydroxyl absorbance (4470 cm^{-1}). To calculate total H_2O contents, peak heights after linear background correction were used together with the linear molar extinction coefficients $\varepsilon_{H2O} = 1.18$ and $\varepsilon_{OH} = 1.14$ l·mol^{-1}·cm^{-1} and the glass density dependence on H_2O concentration $\rho[g·cm^{-3}] = 2.47-0.013·c_{H2O}$ [wt%] (Iacono-Marziano et al. 2007). H_2O concentration profiles were measured perpendicular and parallel to the samples cylinder axis using a motorized XYZ microscope stage and a knife-edge aperture that was set to a measurement

window of 50 × 50 μm. During profile measurements and due to small inter-vesicle distances on a 10 μm scale, the H_2O-filled vesicles in samples with low $\Phi_{glass} < 5\%$ were measured together with H_2O dissolved in the glass in the probed sample volumes. At higher glass porosities, these measurements were not possible, because samples become increasingly opaque with respect to NIR light.

Results

ZrO$_2$ concentration of synthesized glasses

The two glasses VAD79_07 and 08 synthesized using a ZrO_2 ball mill reveal ZrO_2 concentrations of 1200 and 1000 ppm, respectively (Table 1). These values are higher than for the glass that was synthesized using a corundum mill (VAD79_12) with a ZrO_2 concentration of 600 ppm. Note that the given concentrations are mean values of those measurements for which the ZrO_2 concentration was above the detection limit of 350 ppm. For VAD79_07, this was the case in 19 out of 20 measurements, for VAD79_08 in 13 out of 15 analyses, and only 9 out of 20 measurements for VAD79_12. The results indicate that a contamination by 400–600 ppm ZrO_2 by mechanical erosion during milling occurred in glass batches using a ZrO_2 ball mill as compared to the glass using a corundum ball mill for synthesis.

Fe-oxide nanolites

Following the method of Di Genova et al. (2017a, 2018), RMS measurements confirm the absence of a distinct Raman scattering band at 670–690 cm^{-1} (Fig. 2a), indicative of Fe-oxide nanolites, for un-decompressed and decompressed VAD79 samples (2.7 wt% FeO$_{tot}$, 1.37–5.26 wt% H_2O). In contrast, experimental un-degassed and partially degassed hydrous CI samples (4.41 wt% FeO$_{tot}$, Preuss et al. 2016) with $c_{H2O} > 3$ wt% show a distinct Raman band at 680 cm^{-1}. This is consistent with the nanolite occurrence field of hydrous Fe-bearing silicate glasses (Fig. 2b) defined by Di Genova et al (2017a).

Vesicle textures

In all decompressed samples, at the capsule–glass interface, strongly deformed 50–350 μm sized fringe vesicles are present, which increase in size with decreasing P_{final} (Fig. 3). In the central sample volume, vesicles are not observed at 60, 80, and 110 MPa in experiments with c_{H2Oini} of 3.28 (CD93), 4.47 (CD86), and 5.32 wt% (CD48), respectively. In all other samples, the central volume is vesiculated and surrounded by a vesicle-free zone (drainage zone) close to the capsule walls. In samples decompressed with 0.17
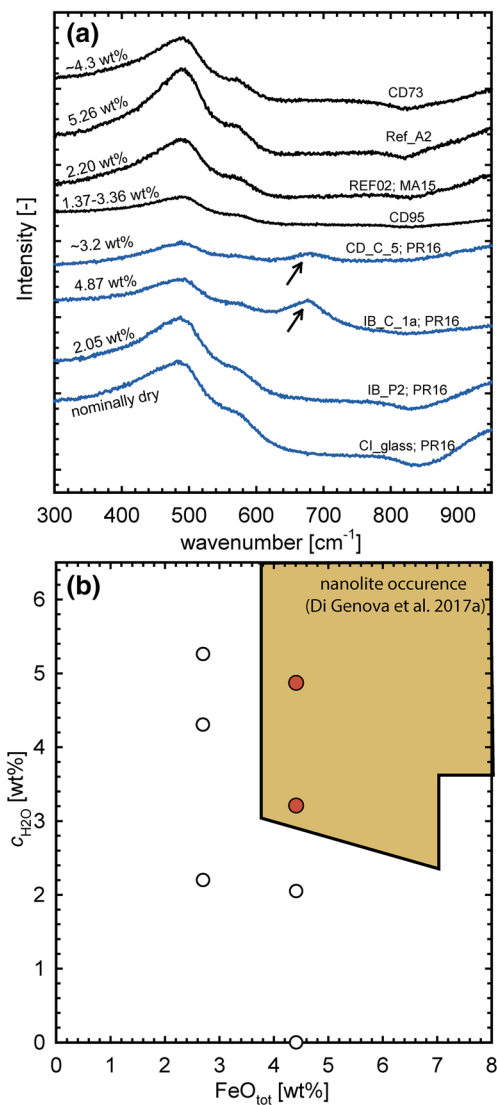
Fig. 2 a Raman spectra of phonolitic VAD79 and trachytic (Campanian Ignimbrite (CI) composition) samples with 2.7 and 4.4 wt% FeO_{tot}, respectively. Numbers at each spectrum are H_2O concentrations (c_{H2O}) in the glasses. In undecompressed and vesicle-free samples (Ref_A2, REF02, IB_C_1a, IB_P2), c_{H2O} was measured with FTIR in transmission. Due to the high glass porosity in the decompressed samples, c_{H2O} of CD73 was determined with Raman microspectroscopy (Allabar et al. 2020) and H_2O concentration given for CD-C-5 is the calculated residual c_{H2O} (Preuss et al. 2016). For CD95, the estimated possible range of c_{H2O} in the glass is given, which is between equilibrium c_{H2O} at P_{final} and T_d and the c_{H2Oini}. At c_{H2O} of 4.87 and ~3.2 wt%, a Raman signal indicative of Fe-oxide nanolites is detected at ~680 cm^{-1} (Di Genova et al 2017a) in samples of CI composition. Fe-oxide nanolites were not detected in the VAD79 samples (black spectra) and the CI samples (blue spectra) with low H_2O contents. References: MA15: Marxer et al. 2015; PR16: Preuss et al. 2016. **b** Fe-oxide nanolite occurrence field (yellow area) determined by Di Genova et al. (2017a). The samples of CI composition in which nanolites were detected (filled, red circles) fall into the area. All samples with c_{H2O} and FeO_{tot} concentrations outside this area do not show Raman bands indicative of Fe-oxide nanolites, consistent with the results of Di Genova et al. (2017a)

$MPa \cdot s^{-1}$, the drainage zone width increases with c_{H2Oini} from ~250 μm at 3.3 wt% to ~500 μm at 4.3 and 5.3 wt% and ~650 μm at 6.5 wt% (Fig. 3), due to increased H_2O diffusivity. These values were determined for samples with low Φ_{glass}, because the drainage zone thins out, as the porosity in the vesiculated sample volume and the fringe vesicles increase the total sample volume. Furthermore, the drainage zone becomes thinner in case of a second phase separation event, located close to the main population (see description below). On the other hand, the drainage zone width increases with decreasing decompression rate due to increased time for H_2O diffusion as shown in Allabar and Nowak (2018).

The central vesiculated volumes in samples with $c_{H2Oini} < 5.6$ wt% contain a high number density of homogeneously dispersed small vesicles, which are similarly sized within each sample (further referred to as main vesicle population). In the experiments with the lowest P_{final} (CD85, CD95, CD73), some vesicles of the main population are observed to be connected to each other. Additionally, in these samples, larger vesicles are observed within the main vesicle population (Fig. 3). Some of the large vesicles are connected to vesicle-free streaks underneath (e.g. CD73, Fig. 3) and are surrounded completely by a vesicle-free drainage zone ~50 μm in width.

In addition to the main vesicle population, which fills most of the central sample volume, in CD87, CD85, CD91, and CD73, a population of smaller vesicles (second population) is observed. Vesicles of the second population are located between the central vesiculated volume and the drainage zone of the capsule wall or in the drainage zone of large vesicles in CD85 and CD73 (Fig. 4), but always close to the main vesicle population.

At 6.3 wt% c_{H2Oini} and a P_{final} of 150 MPa (CD102), vesicles are observable only in the top half of the sample volume at the limit of optical resolution. During further decompression, a pervasive vesiculation throughout the central capsule volume is observable in sample CD101, which was decompressed to a P_{final} of 145 MPa (bright area in the center of the sample in Fig. 3). Eventually, at 120 MPa, less but significantly larger vesicles remain (CD 97). The same pattern is observed in samples with slightly lower c_{H2Oini} of 5.96–5.77 wt%, with half of the sample vesiculated at a P_{final} of 140 MPa. At a P_{final} of 100 MPa (CD100), only small vesicle clouds with finely dispersed vesicles are observed, while the remaining central sample volume contains a low number of large vesicles. In CD44, decompressed at high T_d of 1523 K, half of the sample volume shows finely dispersed vesicles, while the other half contains some large vesicles.

## *VND* and glass porosity

A systematic dependence of *VND* with decompression rate is lacking for hydrous VAD79 melt with c_{H2Oini} of ~5.3 wt%,
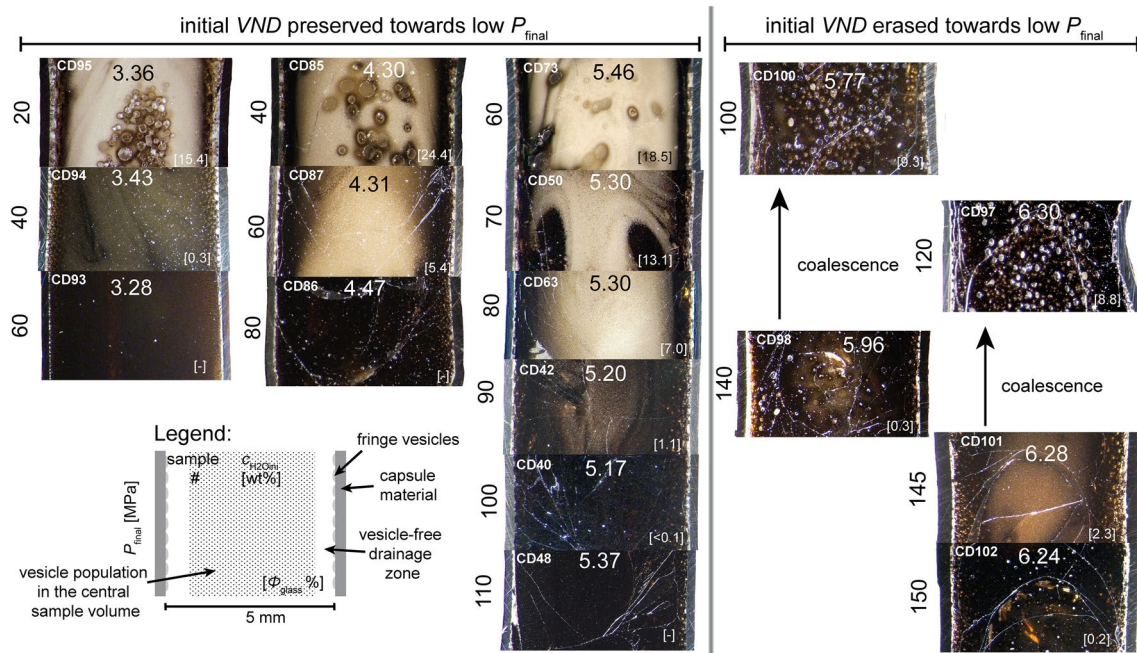
Fig. 3 Details of reflected light images of the experimental samples of the C-Series at constant decompression rate of 0.17 MPa s^{-1}, different P_{final} and c_{H2Oini} ranging between 3.3 and 6.3 wt%. Sample images reflect the sample orientation during the experiments. For illustration purposes, not all samples of the C-Series are shown. *VND*s of the samples are given in Table 2. Full sample images are provided in the online resource "Sample images"
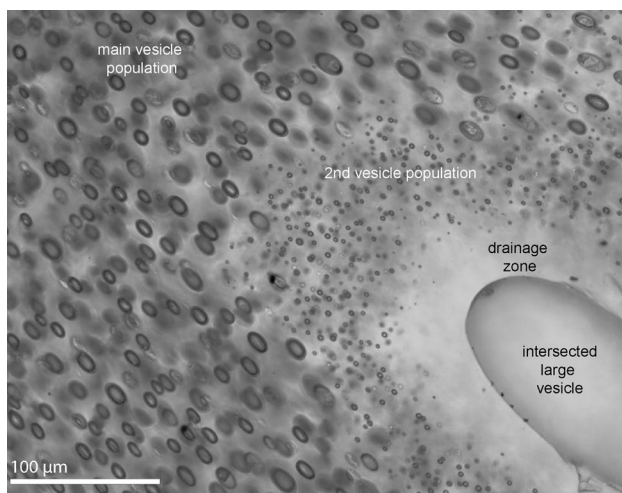

Fig. 4 Transmitted light microscopy image of CD73 thin section in the central vesiculated sample volume. Between the main vesicle population and the intersected large vesicle, a transition zone is visible, which consists of the drainage zone of the large vesicle and a second vesicle population with a lower Φ_{glass} of 9% and higher log-*VND* of 6.07 compared to the main population with log*VND* = 5.41 and Φ_{glass} of 18.5%. Black points at the edge of the large intersected vesicle are artifacts from preparation on the sample surface

as already shown by Allabar and Nowak et al. (2018) for the d*P*/d*t* range of 0.024–10 MPa·s^{-1}. The additional experiment CD28 of this study, with a log*VND* of 5.05, matches with their range of log*VND* from 4.83–5.39, irrespective of decompression rate. The log*VND*s of the additional experiments performed at 1373 K ranging between 4.60 and 4.98 are lower (TD and T-series; Fig. 5) except for one experiment with a log*VND* of 5.48 (CD59). At 1523 K (CD44), log*VND* increased to 5.87, however at slightly lower c_{H2Oini} of 4.96 wt%. The standard deviation of log*VND* is 0.26, as derived from data of the experiments performed at 1373 K and similar c_{H2Oini} of ~ 5.3 wt%. For experiments of the C-Series with c_{H2Oini} ~ 5.3 wt% and different P_{final}, the standard deviation of log*VND* is 0.34. This defines an experimental error in log*VND* of ~ 0.3 log units that is larger than the estimated analytical error of ± 0.13 (error bars in Fig. 5).

Significant changes in *VND* result from experiments with varying c_{H2Oini}. The highest log*VND*s of 5.96 and 6.37 are observed in samples with c_{H2Oini} of ~ 3.3 wt% (Fig. 5). The log*VND* decreases to ~ 5 at c_{H2Oini} of 5 wt%. Towards c_{H2Oini} of ~ 6.3 wt%, the log*VND* increases again to ~ 5.8. In contrast, the *VND* keeps constant within error with decreasing P_{final} for experiments with constant c_{H2Oini} (see online resource "Supplementary information"). Thus, the *VND* is dependent only on c_{H2Oini} and slightly on T_d. In the experimentally investigated P_{final} range, Φ_{glass} of the main population increases with decreasing P_{final} from < 0.1 to a maximum of 15.4, 24.4, and 18.5% at ~ 3.3, ~ 4.4, and ~ 5.3 wt% c_{H2Oini}, respectively (Table 2).
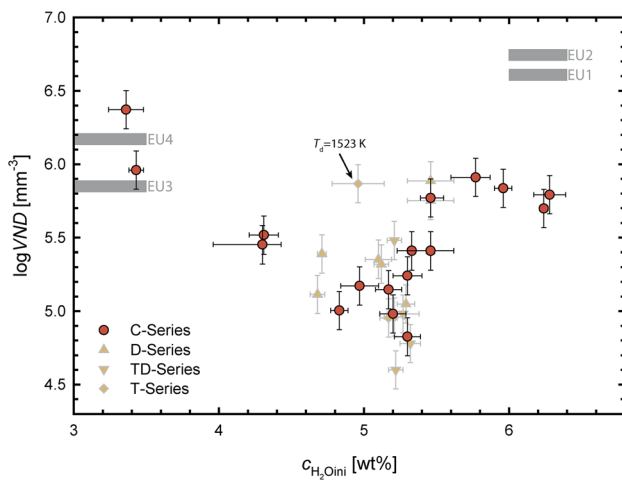
Fig. 5 logVND (vesicle number density) of the main vesicle populations within the central sample volume vs. initial H_2O concentration (c_{H2Oini}). The VND shows a minimum at c_{H2Oini} of ~5 wt% and increases towards lower and higher c_{H2Oini} up to 1.5 log units. Experiments with various decompression rates (D-series) and similar c_{H2Oini} ranging between 4.68 and 5.46 wt% reveal no systematic change of VND similar to the T-Series experiments with increased T_d of 1373 K. A substantially higher T_d of 1523 K, however, results in a significantly higher logVND. The grey bars indicate the mean logVNDs and the corresponding pre-eruptive H_2O concentrations derived from melt inclusions (Cioni 2000) of white (EU1 and EU2) and grey pumice (EU3 and EU4) of the AD79 Vesuvius eruption (Gurioli et al. 2005; Shea et al. 2010a)

The logVNDs of the second population of vesicles (Table 2) ranging between 5.66 and 6.14 are significantly higher than the logVND of the respective main populations of 5.41–5.45. The Φ_{glass} within the volume of the second vesicle population ranging between 0.2 and 9.0% are lower than the values of the respective main population ranging between 9.0 and 24.4%. In sample CD73, the second population shows a higher Φ_{glass} in the drainage zone of the large vesicle (9.0%, Fig. 4) compared to the second population located in the capsule wall drainage zone (1.0%).

H_2O concentrations

The H_2O concentrations as measured by FTIR (c_{H2OIR}) of the central sample volumes without observable vesicles resemble the initial $c_{H2Ograv}$. The same holds for the samples with $\Phi_{glass} < 5\%$, where the probed volume contained glass together with vesicles (e.g., CD-C-23, CD40). In three experiments, considerable weight loss occurred during welding. For two of these samples (CD102 and CD101), c_{H2OIR} is similar to $c_{H2Ograv}$, whereas CD98 has a reduced c_{H2OIR} of 5.96 wt% as compared to the $c_{H2Ograv}$ of 6.27 wt%. In CD44, the c_{H2OIR} measured in the central vesiculated sample volume is slightly decreased to 4.96 wt% with respect to the $c_{H2Ograv}$ of 5.28 wt%. For CD85, which also experienced

weight loss during welding, the porosity was too high for reliable c_{H2OIR} determination. The c_{H2OIR} measured in the volumes of the second population of vesicles are within error similar to the $c_{H2Ograv}$ in CD87, CD85, and CD91, but decreased considerably to 4.99 wt% in CD73 compared to the $c_{H2Ograv}$ of 5.46 wt%.

Discussion

H_2O concentrations

In experiments starting from slightly undersaturated conditions, the c_{H2Oini} is defined by the gravimetrically determined $c_{H2Ograv}$. However, since, for samples with $\Phi_{glass} < 5\%$, the c_{H2OIR} equals within error $c_{H2Ograv}$ (e.g., CD-C-23, CD40; Table 2), c_{H2OIR} was used as the dissolved H_2O concentration in the melt prior to decompression (c_{H2Oini}). This has the advantage that uncertainties in $c_{H2Ograv}$, caused by weight loss during welding, are eliminated (e.g., CD102, CD98). The c_{H2OIR} reveal that weight loss of CD102 and CD101 resulted from Au80Pd20 loss during welding, whereas in case of CD98, some H_2O was lost. Similar to CD77 (Allabar and Nowak 2018), the c_{H2O} prior to phase separation in CD44 was already reduced as compared to the $c_{H2Ograv}$. During decompression at a higher T_d of 1523 K, the H_2O diffusivity is higher and viscosity is lower than at a lower T_d of 1323 K. Thereby, diffusional loss of H_2O into fringe vesicles, that early nucleated heterogeneously at the capsule wall during decompression, increases and ascent of fringe vesicles is facilitated. Both effects reduce H_2O supersaturation within the central sample volume, similar to CD77 with a low decompression rate of 0.024 MPa·s^{-1} (Allabar and Nowak 2018). However, in both samples, a reduced but constant c_{H2OIR} was measured in the central vesiculated sample volume, which was therefore used as c_{H2Oini}.

For CD100, a mean c_{H2OIR} of 5.43 wt% was measured in various small vesicle clouds. Because the vesicle clouds of the main vesicle population are only small (~0.1 mm^3), it may be possible that after phase separation of the main vesicle population, H_2O was lost into large vesicles which are located close to the small vesiculated melt volumes, driven by Ostwald ripening. Because CD98 with a similar c_{H2Oini} shows that the melt was vesiculated by the main population at higher P_{final}, it is suggested that the high VND observed in the small vesicle clouds in CD100 represents the product of a phase separation at the initial c_{H2O}. Therefore, c_{H2Oini} of 5.77 wt% is assumed for CD100.

In decompression experiments that started from H_2O supersaturated conditions after hydration (e.g., CD83 and CD73), c_{H2Oini} is defined by the H_2O solubility at P_{start} and T_d. Solubility data for hydrous VAD79 melt at T_d and

P_{start} were derived from Iacono-Marziano et al. (2007) and Marxer et al. (2015). The $c_{H2Ograv}$, c_{H2OIR}, and H_2O solubility data that were used as c_{H2Oini} are highlighted in bold numbers in Table 2.

Results of c_{H2OIR} measurements in the glass between vesicles are presented in Allabar et al. (2020). These data are not used for further discussion here, because the c_{H2OIR} of the glass between vesicles does not represent c_{H2O} dissolved in the melt at P_{final} prior to quench due to H_2O resorption from the fluid phase back into the melt during quench (McIntosh et al. 2014; Allabar et al. 2020).

Phase separation

Verification of homogeneous phase separation

With the decompression experiments compiled and performed for this study, it is intended to investigate homogeneous phase separation of hydrous phonolitic melt. Therefore, it is necessary to verify a single-phase superliquidus system at the onset and during decompression until vesicle formation starts in the central volume of the sample.

The use of a ZrO_2 ball mill for synthesis of the starting glasses VAD79_03-10 caused ZrO_2 contamination of 1000–1200 ppm, while the use of a corundum ball mill for synthesis of VAD79_12 yields a lower ZrO_2 contamination of 600 ppm ZrO_2. ZrO_2 saturation caused by ZrO_2 contamination could lead to pre-existing ZrO_2 or $ZrSiO_4$ crystals or ZrO_2 rich domains on a mesoscopic scale (e.g., Cormier et al. 2015; Dargaud et al. 2011). Zr phases may act as vesicle nucleation sites, favoring heterogeneous nucleation of vesicles during decompression. However, a ZrO_2 solubility of 3660 ppm was calculated for dry VAD79 melt composition at 1323 K using the model of Gervasoni et al. (2016). The ZrO_2 solubility increases linearly with H_2O concentration up to 2 wt% and remains constant towards higher c_{H2O} in granitic melts at high T (Watson and Harrison 1983). Assuming a similar dependence in phonolitic melt, the measured ZrO_2 concentrations in the starting glasses are far below the ZrO_2 saturation limit. Furthermore, pre-existing crystals in the starting glasses or crystal formation during degassing caused by ZrO_2 contamination were not observed by TLM or SEM-BSE imaging. Experimental samples with high and low ZrO_2 contamination with identical decompression conditions of c_{H2Oini} ~ 5.3 wt%, dP/dt of 0.17 MPa·s^{-1}, and P_{final} of 80 MPa reveal similar VNDs. The samples CD63 (starting glass VAD79_07) and CD91 (starting glass VAD79_12) reveal logVNDs of 5.24 and 5.41, respectively.

Aside from Zr phases, Fe-oxide crystals may form during the decompression experiments at the lowest T_d of 1323 K. Surfaces of magnetite crystals reduce efficiently the energy and the supersaturation pressure required for H_2O vesicle nucleation (e.g., Hurwitz and Navon 1994;

Shea 2017). H_2O solubility experiments of Iacono-Marziano et al. (2007) reveal that at P between 250 and 30 MPa, the phase boundary of Fe-oxides for VAD79 melt is between 1323 and 950 K. This is supported by the synthesis of hydrous reference VAD79 samples of Marxer et al. (2015) at 1323 K, 200–75 MPa and intrinsic oxygen fugacity of ΔlogQFM = +3.5. BSE images reveal that these glasses are free of μm-sized Fe-oxide crystals. Phase equilibria experiments with hydrous CI melts of similar composition, determined by Fabbrizio and Carroll (2008) at ΔlogNNO = +0.8, reveal liquidus temperatures higher than 1143 K and 1133 K for P of 50 and 200 MPa, respectively. However, experiments at $T > 1143$ K that are required to bracket the phase boundary for the liquidus phase magnetite are lacking. Fanara et al (2012) performed phase equilibria experiments with hydrous CI melt in an IHPV at intrinsic ΔlogQFM = +3.5. The liquidus temperature, defined by the phase boundary of magnetite, is between 1273 and 1323 K for H_2O activities between 1 and 0.5 and a P of 200 MPa. These data show that for hydrous VAD79 melt, the phase boundary of magnetite may be close to the lowest decompression temperature of 1323 K.

Another driving mechanism for decompression-induced vesicle formation in hydrous melt might be heterogeneous nucleation at nanometer-sized Fe-oxide crystals (ultrananolites smaller than 30 nm and nanolites 30 nm to 1 μm as classified by Mujin et al. 2017), as suggested by, e.g., Di Genova et al. (2017a,b; 2018) and Shea (2017). Such nanolites are observed in natural volcanic products. The formation of Fe-oxide nanolites can be related to pre-, syn-, and post-eruptive processes. Post-eruptive Fe-oxide nanolites are observed in glass particles of welded tuff (Schlinger and Smith 1986; Schlinger et al. 1988) and in natural obsidian glasses (Sharp et al. 1996). Fe-oxide nanolites related to syn-eruptive processes are observed in dense juvenile fragments of lava derived from a 2011 sub-plinian andesitic–dacitic eruption of Shinmoedake (Mujin and Nakamura 2014 and Mujin et al. 2017). Fe-oxide nanolites at and near vesicle surfaces of Mt Etna ashes might be related to syn- and post-eruptive processes (Barone et al. 2016). Furthermore, Di Genova et al. (2017a; b; 2018) observed Fe-oxide nanolites in experimental and natural hydrous silicate glasses.

Fe-oxide nanolites potentially drive heterogeneous vesicle nucleation that may have been overlooked in previous studies of Iacono-Marziano et al. (2007), Marxer et al. (2015) Preuss et al. (2016) and Allabar and Nowak (2018), because this mechanism may mimic homogeneous phase separation. Fe-oxide nanolites may form during thermal equilibration prior to decompression and during decompression and degassing of hydrous VAD79 melt. Nanolite formation might be induced by thermodynamic metastability or instability of H_2O supersaturated melt and by increasing liquidus temperature with decreasing H_2O content.

However, the RMS measurements (Fig. 2) prove that the selected quenched hydrous VAD79 samples are free of Fe-oxide nanolites. The minimum decompression temperature of 1323 K for our VAD79 experiments is sufficiently high to inhibit Fe-oxide nanolitization prior to and during decompression and phase separation, and during cooling the samples. This holds even for the sample CD95 with the lowest c_{H2Oini} of 3.36 wt% c_{H2Oini} and P_{final} of 20 MPa (Fig. 1) that experienced a T drop of 50 K at the end of decompression. Thus, the vesicle formation in hydrous VAD79 melt is not affected by Fe-oxide nanolitization.

In contrast to the VAD79 samples, the CI samples containing 4.87 and ~3.2 wt% H_2O (Preuss et al. 2016) show distinct Raman bands at ~680 cm^{-1}, indicative of Fe-oxide nanolites. However, both hydrous melt compositions reveal logVNDs in the same order of magnitude of 4.83–5.92 during decompression, independent of decompression rate (Preuss et al. 2016; Allabar and Nowak 2018) and independent of the occurrence of Fe-oxide nanolites in the quenched glasses. This suggests that (1) the Fe-oxide nanolites, detected in hydrous Campi Flegrei trachytic glass samples of Preuss et al. (2016), formed after decompression and vesicle formation during rapid isobaric quench within the metastable field of the hydrous supercooled melt or (2) that Fe-oxide nanolites in CI melts formed prior to phase separation, e.g., deep within the metastable field of supersaturated melt, and mimic homogeneous vesicle formation.

We conclude that heterogeneous vesicle nucleation at low supersaturation occurred only at the interface of capsule walls and melt as an experimental artifact (fringe vesicles) in our samples. A vesicle-free drainage zone evolved between fringe vesicles and the central sample volume by diffusional H_2O loss into fringe vesicles during further decompression after their formation. If heterogeneous nucleation had also formed the observed vesicles in the central sample volume, this vesicle-free drainage zone would be smaller due to much lower supersaturation P required for heterogeneous nucleation and the shorter time available for H_2O diffusion into fringe vesicles (Allabar and Nowak 2018). At a ΔP_{het} (difference between saturation P and pressure of heterogeneous vesicle nucleation) of ~5 MPa that is suggested for nucleation at magnetites (Hurwitz and Navon 1994; Shea 2017), the drainage zones would be only ~120 μm for 6.3 wt% c_{H2Oini} to ~75 μm at 3.3 wt%. The observed drainage zone width of 650 and 250 μm, respectively, is indicative of homogeneous phase separation at larger supersaturations at the pressure at which phase separation starts (P_{hom}). Finally, for heterogeneous nucleation, a dependence of VND on dP/dt, as predicted by nucleation theory, is still expected (Shea 2017; Allabar and Nowak 2018). However, this is not observed in hydrous phonolitic melt.

In summary, in the decompression experiments of this study and in the published experiments compiled in this study, it is ensured that homogeneous phase separation by vesicle formation occurred in the central volume of the samples as close to the terminus as possible. Therefore, only the main vesicle population was considered for characterization of homogeneous phase separation by quantitative VND analysis.

Homogeneous phase separation

Homogeneous phase separation occurred in the central volume of the samples where the c_{H2Oini} was preserved and not affected by diffusional H_2O loss towards heterogeneously nucleated vesicles at the capsule walls. Allabar and Nowak (2018) showed that an independence of VND on decompression rate cannot be explained by nucleation theory, but is consistent with the theory of spinodal decomposition.

For vesicle nucleation, a continuous increase of VND with decreasing P_{final} is expected until a sufficiently high number of vesicles is formed to decrease supersaturation below a threshold value for further nucleation. This leads to a broadening in vesicle size distribution towards low decompression rates (Shea et al. 2010b). However, the observed independence of VNDs with decreasing P_{final} at constant c_{H2Oini}, the similarly sized vesicles in the central sample volume within each experiment (see VVD-plots in the online resource "Supplementary information"), and the independence of VND from decompression rate (Allabar and Nowak 2018) indicate that the formation of vesicles is inconsistent with nucleation theory. It is suggested that off-critical spinodal decomposition is a potential phase separation mechanism in H_2O supersaturated phonolitic melt (Allabar and Nowak 2018). Spinodal decomposition is a non-activated spontaneous process at the spinode, i.e., at the thermodynamic limit of metastability (e.g., Cahn and Hillard 1959; Cahn 1965). Thermally induced spatial concentration (c) fluctuations are attenuated by downhill diffusion in the metastable state, where the second derivative of the free energy of mixing (ΔG) $\partial^2 \Delta G/\partial c^2$ is > 0. In the unstable state, however, where $\partial^2 \Delta G/\partial c^2$ is < 0, the concentration fluctuations are amplified by uphill diffusion until sharp phase boundaries between hydrous silicate melt and an H_2O-rich fluid phase evolve (Debenedetti 2000; Tanaka et al. 1990).

A quantitative approach, based on the theory of spinodal decomposition, to explain the observed minimum of VND at a c_{H2Oini} of ~5 wt% (Fig. 5) is difficult, because H_2O is a reactive component in silicate melts. The volatile component H_2O dissolves mainly as hydroxyl groups and as some molecular H_2O, which was demonstrated by in-situ measurements of hydrous aluminosilicate melt (Nowak and Behrens 1995; Nowak and Behrens 2001). The polycondensation reaction 2(Si,Al)-OH = (Si,Al)-O-(Si,Al) + H_2O produces molecular H_2O during phase separation and is accompanied by an exothermic reaction enthalpy (Nowak and Behrens

2001), in addition to the enthalpy and entropy of mixing. Thus, the phase separation cannot be quantified by a simple regular solution model as conceptually presented by Allabar and Nowak (2018). However, a sound physicochemical quantification of spinodal phase separation of hydrous phonolitic melt is beyond the scope of this study. Regardless of these limitations, a qualitative justification for the observed dependence of *VND* on c_{H2Oini} is possible for two different assumptions:

(1) It is possible that the observed *VND* is defined by the wavelength of concentration fluctuations that are amplified during spinodal decomposition. In this case, vesicles are formed one wavelength apart from each other. Such a case is described for droplet-type spinodal decomposition, which is possible when the volume fraction of the minor phase, H_2O in the case of hydrous melt, is < 15% (Cahn 1965). The critical (i.e., minimum) wavelength (λ_c) that is amplified when a system becomes unstable is $\lambda_c = 2\pi/\beta_c$, where the critical wavenumber β_c is defined as (Cahn 1965):

$$\beta_c = \left(\frac{-\partial^2 \Delta G/\partial c^2}{2\kappa} \right)^{\frac{1}{2}}, \tag{1}$$

where κ is a positive constant and the numerator term is the curvature of the free energy curve as a function of composition at given *P* and *T*. The wavenumber, at which amplification is maximum, is $\beta_m = \beta_c/(2^{0.5})$. Consequently, at given *P* and *T*, the wavelength of successfully amplified concentration modulations, which may be associated with the observed *VND*, depends on composition, i.e., on the H_2O concentration. In our experiments, not only the c_{H2Oini} is varied, but as a consequence, also the P_{hom}. This could lead to the increase of *VND* towards high and low c_{H2Oini}. The higher *T* of 1523 K of CD44, compared to all other experiments, could have induced a similar change in curvature of the free energy curve as the increase or decrease in c_{H2Oini}, leading to a higher *VND* (Fig. 5).

(2) Alternatively, the *VND* observed in the experimental samples may be the result of textural coarsening of fractal ramified structures (Cahn 1965) of the two phases, into which the hydrous melt may have separated by spinodal decomposition. Since the samples that were quenched at different P_{final} show similar *VND*s at constant c_{H2Oini}, there might be a stable *VND* at which coarsening stops. Coarsening likely depends on melt viscosity, surface tension, and H_2O diffusivity, which are all parameters that depend on H_2O concentration. This could result in the varying *VND* with changing c_{H2Oini}.

Evolution of degassing

For all vesiculated samples, Φ_{glass} is smaller than the calculated Φ_{equ} at P_{final} and T_d (Allabar et al. 2020). At first sight,

this suggests disequilibrium degassing during decompression. However, diffusion calculations reveal that near equilibrium must have been approached in all experiments due to sufficiently high H_2O diffusivity and small inter-vesicle distances at a 10 μm scale (Allabar et al. 2020). Only for the samples with ~ 3.3 wt% c_{H2Oini}, degassing close to equilibrium is not ensured during decompression to P_{final} (Allabar et al. 2020). For all other experiments, the low Φ_{glass} compared to Φ_{equ} is suggested to be related to vesicle shrinkage during isobaric cooling caused by the decrease of the molar volume of the H_2O fluid during cooling (Marxer et al. 2015), accompanied by resorption of H_2O from fluid vesicles back into the melt (McIntosh et al. 2014) due to increasing H_2O solubility with decreasing *T* (e.g., Schmidt and Behrens 2008). The suggestion of significant vesicle shrinkage is supported by the observation of strongly deformed fringe vesicles. Vesicle shrinkage during cooling of the samples from this study is in detail explained in Allabar et al. (2020). However, the c_{H2Oini}-dependent *VND*s and coalescence processes can be discussed here, without considering vesicle shrinkage.

At $c_{H2Oini} < 5.6$ wt%, the initially formed *VND* of the vesicles of the main population remains stable during decompression to low pressure until Φ_{melt} is sufficiently large for the onset of coalescence, as observed in the experiments with P_{final} of 20, 40, and 60 MPa with 3.36 (CD95), 4.30 (CD85), and 5.46 wt% (CD73) c_{H2Oini}, respectively (Fig. 6). It can be excluded that the larger vesicles observed in the central part of the samples are due to pre-existing vesicles that might result from air vesicles in the glass cylinders used for the decompression experiments (Preuss et al. 2016). In this case, the vesicle-free drainage zone around these vesicles should be as wide as the drainage zone towards the capsule wall, which is not the case (Fig. 3). In CD95, the drainage zone towards fringe vesicles at the capsule wall is ~ 400 μm, while the distance between the walls of large vesicles and the main population is only ~ 50 μm. This suggests that the large vesicles in the central volume of the samples may be former fringe vesicles that detached from the capsule walls and ascended through the melt during further decompression and degassing. Vesicle-free streaks, indicating the ascent track of these vesicles, are visible, e.g., in CD73 (Fig. 3). However, in CD95 and CD85, large vesicles are isolated in the center of the samples and surrounded by small vesicles. Ascent tracks below these large vesicles are not visible. Additionally, the observation that at $P_{final} > 20$ and > 40 MPa large vesicles are not present in central sample volumes with c_{H2Oini} of 3.3 and 4.3 wt%, respectively, argues for coalescence, forming the large vesicles from the main vesicle population at the lowest P_{final}. Assuming Φ_{equ} (calculated after Gardner et al. 1999, Eq. 5 therein) prior to quench (Allabar et al. 2020), it can be concluded from the experimental observations that coalescence and the linked
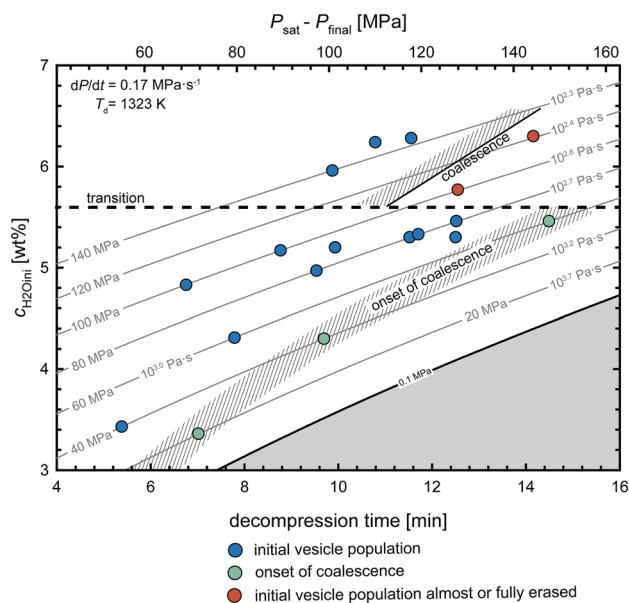
Fig. 6 Experimental parameters and textural features of the C-Series plotted for initial H_2O concentration (c_{H2Oini}) vs. decompression time [(saturation pressure (P_{sat})-final pressure (P_{final}))/(dP/dt)] for a dP/dt of 0.17 MPa·s^{-1} and a decompression temperature of 1323 K. The grey lines indicate the P_{final} in MPa and the corresponding melt viscosity in case of equilibrium degassing calculated after Giordano et al. (2008). The colors of symbols indicate the stage of vesicle coalescence observed in the experiments. A transition in degassing evolution occurs at c_{H2Oini} of 5.6 wt%. Below 5.6 wt% c_{H2Oini}, the initial *VND* (vesicle number density) is preserved to relatively low P_{final} until the onset of coalescence is observed. In this case, the *VND* is likely preserved until magma ejection to the surface in case of a natural system, where decompression rate accelerates while degassing proceeds (Proussevitch and Sahagian 1996). Note that equilibrium degassing is not ensured in the experiment decompressed with c_{H2Oini} of ~3.3–20 MPa (Allabar et al. 2020). Thus, the actual melt viscosity may be slightly lower than the given value for equilibrium c_{H2O} for this experiment. At c_{H2Oini} > 5.6 wt%, vesicle coalescence occurs at higher (P_{sat}-P_{final}), i.e., higher c_{H2O} and lower melt viscosity. *VND* is significantly reduced and during further decompression it is likely that H_2O supersaturation builds up in interstitial melt volumes due to large inter-vesicle distances, causing a possible second-phase separation event at c_{H2O} < c_{H2Oini}

reduction of *VND* of the main vesicle population starts at similar Φ_{melt} of 30–50%, 30–40%, and 35–40%, at 3.3, 4.3, and 5.3 wt% c_{H2Oini}, respectively. Note that the Φ_{melt} values for 3.3 wt% c_{H2Oini} are prone to the uncertainty whether near-equilibrium degassing occurred in CD95 (Allabar et al. 2020). In case of disequilibrium degassing, the Φ_{melt} at the onset of coalescence would be lower.

The vesicles of the second population formed when H_2O diffusion into the large vesicles or fringe vesicles and towards the opposite side into vesicles of the main population was not fast enough to effectively reduce the H_2O supersaturation that had built up during further continuous decompression. This led to a secondary homogeneous phase

separation event at c_{H2O} < c_{H2Oini} and lower P_{final} as compared to the main vesicle population, resulting in lower Φ_{equ} and consequently lower Φ_{glass}. The log*VND* of the second population is 0.21–0.69 log units higher than the log*VND* of the respective main population. This is consistent with an increase of *VND* towards lower c_{H2O} of the melt just prior to phase separation (Fig. 5).

However, this observation contrasts with the measured c_{H2OIR} of the volumes of the second population, which mostly reflects within error the c_{H2Oini} (Table 2). The measured c_{H2OIR} could in this case overestimate the c_{H2O} of the melt at phase separation. As described in Allabar et al. (2020), H_2O is resorbed from the fluid back into the melt during quench. As a result, the $c_{H2Omelt}$ at T_d and P_{final} is lower than $c_{H2Oglass}$ between vesicles at ambient conditions. In the large volume of the main vesicle population, the H_2O is resorbed rapidly into the melt from the vesicles during cooling due to short inter-vesicle distances on a 10 μm scale. Thus, the measured c_{H2OIR} is expected to reflect the c_{H2Oini} and thus the c_{H2O} at phase separation. In the small volume of the second population, which is always located close to the main vesicle population, H_2O may not only be resorbed from the vesicles of the second population but also from the main population into the melt volume of the second population. As a result, the measured c_{H2OIR} in the glass is higher than the c_{H2O} at phase separation.

At c_{H2Oini} of 5.6 wt% a transition is observed in the degassing evolution during decompression (Fig. 6). At c_{H2Oini} > 5.6 wt%, the initial *VND* of the main population is only observable for a short *P* interval of, e.g., ~20 MPa at 6.3 wt% c_{H2Oini}. In CD102 (P_{final} = 150 MPa), only in half of the sample, vesiculation is observable at very low Φ_{glass}, which is first due to the large drainage zone at high c_{H2Oini}, that is better visible in CD101 (Fig. 3) due to the higher Φ_{glass}. Second, vesicles in CD102 could have shrunk and H_2O may have been resorbed back into the melt during cooling (Allabar et al. 2020), so that this experiment may be at the very limit of vesicle observation for the used quench rate. During decompression from 150 to 145 MPa (CD101), the initially observed log*VND* remains stable at ~5.7. During further decompression to 120 MPa, the main vesicle population is completely erased by coalescence and a low log-*VND* of 1.92 remains (CD97) at decompression times ((P_{sat}-P_{final})/(dP/dt)) at which the initial *VND* is still observed at c_{H2Oini} < 5.6 wt% (Fig. 6). The *P* range of 145–120 MPa, during which *VND* drastically decreases at 6.3 wt% c_{H2Oini}, corresponds to Φ_{melt} (= Φ_{equ}) between 15 and 21% for equilibrium degassing of the homogeneously formed vesicles of the main population. Therefore, coalescence occurs at much lower melt porosities and to a greater extent at 6.3 wt% compared to c_{H2Oini} < 5.6 wt%. In experiments with c_{H2Oini} < 5.6 wt%, where the onset of coalescence is observed at 20, 40, and 60 MPa with increasing c_{H2Oini}, logη (in Pa·s) calculated

for equilibrium c_{H2O} at 1323 K is 3.7, 3.2, and 3.0 (Giordano et al. 2008), respectively (Fig. 6). Note that the first value for 3.3 wt% c_{H2Oini} may be lower in case of possible disequilibrium degassing. Beyond the transition at c_{H2Oini} of 5.6 wt%, the initial vesicle population is already completely erased at lower decompression time, i.e., lower logη of 2.4–2.6. The early onset of coalescence at $c_{H2Oini} > 5.6$ wt% is attributed to the lower viscosity with increased c_{H2O}. Decreasing viscosity favors coalescence (i.e., Fortelný et al. 1999). Consequently, at a decompression rate of 0.17 MPa·s^{-1}, the initial *VND* cannot be preserved during further continuous decompression.

Implications for volcanic eruptions

During the 79AD Vesuvius eruption, grey (tephriphonolite) and white (phonolite) pumice were ejected and are recorded in distinct eruptive units (EU) (e.g., Cioni et al. 1995). One may assume that small differences in bulk composition between white and grey pumice do not significantly influence the degassing behavior, as shown by Preuss et al (2016) for VAD79 white pumice and trachytic CI composition.

For the melt that formed the natural Vesuvius white pumice, a c_{H2Oini} of 6.0–6.4 wt% was determined in melt inclusions in samples of eruptive unit 2 (EU2) (Cioni 2000). For EU1, pre-eruptive H$_2$O concentration data are lacking. However, chemical bulk compositions of EU1 and EU2 are similar, and a homogeneous H$_2$O distribution in the magma that formed the white pumice is assumed (Shea et al. 2014). Therefore, the c_{H2Oini} of EU1 is suggested to be similar to EU2. The log*VND* in the white pumice ranges from 6.41 to 6.89 in EU1 and 6.38–7.08 in EU2 with mean values of 6.61 and 6.74, respectively (Shea et al. 2010a; Gurioli et al. 2005; Fig. 5). However, pre-eruptive T was ~ 1100–1200 K (Shea et al. 2009), well below the experimental temperatures, which results in partial crystallization and a higher melt viscosity by one log unit (Giordano et al. 2008) at the given c_{H2Oini}.

EU1 and EU2 reveal higher *VND*s than the experimental initial *VND* for similar c_{H2Oini} (Fig. 5). Furthermore, in the experiments with $c_{H2Oini} > 5.6$ wt%, the initial main population is erased at relatively high P during decompression at 1323 K (Fig. 6). However, at the lower magmatic temperature, it is possible that coalescence is shifted to lower P, due to higher viscosity compared to the superliquidus decompression experiments. Thus, the high *VND* in EU1 and EU2 may still represent the main vesicle population. Two possible scenarios may explain the high *VND* in natural white pumice, both considering pre-existing vesicles prior to homogeneous phase separation (Allabar and Nowak 2018), because vesicles may heterogeneously nucleate at low supersaturation (Hurwitz and Navon 1994; Shea 2017) on crystal surfaces in a subliquidus melt. These pre-existing vesicles

drive buoyant acceleration of magma ascent and decrease melt c_{H2O} in their vicinity by H$_2$O diffusion. The assumption of a pre-existing vesicles number density, which equals the crystal number density of up to 0.3 mm^{-3} (Iacono-Marziano et al. 2007; Allabar and Nowak 2018), results in a limiting decompression rate for homogeneous phase separation of 0.06 MPa·s^{-1} for a magma with c_{H2Oini} of 6.3 wt% and T of 1150 K. In the first scenario, at decompression rates > 0.06 MPa·s^{-1}, the initial c_{H2O} is preserved in interstitial melt volumes. The observed *VND* of natural white pumice would represent the initial *VND* of homogeneous phase separation that was preserved during magma ascent to the surface. This requires that at lower T of ~ 1150 K, the initially formed *VND* at c_{H2Oini} of ~ 6 wt% *VND* is higher than observed in experiments at 1323 K.

In the second scenario, at decompression rates < 0.06 MPa·s^{-1}, the pre-existing *VND* is sufficient to reduce H$_2$O supersaturation to prevent homogeneous phase separation at high c_{H2O}. The *VND* of white pumice suggests vesicle formation at decreased c_{H2O} values of < 3.3 wt%, at which homogeneous phase separation produced a high *VND*, consistent with the experimental results. In both scenarios, initial and second phase separation events occur that lead to a bimodal vesicle size distribution, as observed in natural products (e.g., Gurioli et al. 2005), and indicate two decompression and vesiculation stages.

The eruptive units EU3 and EU4 consist of grey pumice with a c_{H2Oini} of 3–3.5 wt% (Cioni 2000; Shea et al. 2014). The log*VND*s range from 5.15 to 6.57 in EU3 and 5.97–6.30 in EU4 with mean values of 5.84 and 6.18, respectively (Gurioli et al. 2005; Fig. 5). Due to a pre-eruptive magma T of ~ 1323 K (Cioni et al. 1995) for the grey pumice, the *VND*s are comparable to our experimental results and are in good agreement with the experimentally derived *VND*s (Fig. 5). Thus, we suggest that the high *VND*s in the natural grey pumice represent the initially formed vesicle population that is preserved down to 0.1 MPa and causes porosities up to 80% (Shea et al. 2012) until open system degassing commences. In the superliquidus continuous decompression experiments of this study, the onset of coalescence in samples with c_{H2Oini} of 3.3 wt% was already observed at 20 MPa during decompression with 0.17 MPa·s^{-1} (Fig. 6). However, in a natural system, decompression rate increases at the onset and during vesiculation by increasing buoyancy of the melt with decreasing density. Thus, the time available for coalescence decreases and the initial *VND* is likely preserved until the magma reaches the surface.

Previously, it has been shown that under the assumption of homogeneous nucleation, extreme decompression rates of 50–55 MPa·s^{-1} would be necessary to explain the observed high *VND*s in grey pumice. Therefore, it has been suggested that heterogeneous nucleation on oxides caused the high *VND* observed in grey pumice, for which decompression

rates of 2.35–11.53 MPa·s^{-1} were calculated (Shea et al. 2012). Contrary to that, an alternative explanation is phase separation by spinodal decomposition that may have formed the high *VND*. Micro-phenocrysts, mainly leucite, with high number densities of $\sim 10^4$ formed during degassing (Shea et al. 2012) and are, therefore, not considered as sites for heterogeneous nucleation. Furthermore, we assume that although chlorine is an additional component (~ 0.6–0.8 wt%, Shea 2014) in natural VAD79 magma, the experiments of this study, with solely H_2O as volatile component, may be comparable with the natural system, because a non-volatile behavior of chlorine during the AD79 Vesuvius eruption is observed (Shea et al. 2014). Therefore, the solubility of H_2O in phonolitic–trachytic melt is not largely affected by such low chlorine concentrations (Webster et al. 2014). According to our experimental data, we suggest that 0.17 MPa·s^{-1} is sufficient to form $\sim 10^6$ mm^{-3} vesicles by spinodal decomposition before the onset of an explosive eruption and ejection of the grey pumice.

Conclusion

In addition to the decompression rate independent *VND* (Allabar and Nowak 2018) in superliquidus phonolitic melt, the high *VND* and their dependence on c_{H2Oini} found in this study are also compatible with the theory of spinodal decomposition. However, definite evidence and a quantitative description for this phase separation mechanism are still lacking.

The *VND* finally observed in volcanic products is, particularly for high c_{H2Oini}, likely an obscured product of initial vesicle formation, coalescence, ripening, and secondary-phase separation processes in interstitial melt volumes. The resulting vesicle texture depends on parameters such as melt viscosity and the available timescale, i.e., decompression rate before and during fragmentation and quench. From the comparison of experimental results with natural pumices of the AD79 eruption, the high *VND* in natural products may be explained by homogeneous spontaneous phase separation as in the experiments of this study. However, although the high-temperature experiments of this study are not fully comparable with the VAD79 eruption, they may be similar to the recent magma conditions of Vesuvius. In the last 20 ka, the magma temperature of Vesuvius has continuously increased from ~ 1100 to > 1373 K (Scaillet et al. 2008). Therefore, the results of this study may be useful for the interpretation of future Vesuvius eruptions and eruptions of other volcanoes with phonolitic and trachytic superliquidus melt.

References

Alidibirov M, Dingwell DB (1996) Magma fragmentation by rapid decompression. Nature 380:146–148

Allabar A, Nowak M (2018) Message in a bottle: Spontaneous phase separation of hydrous Vesuvius melt even at low decompression rates. Earth Planet Sci Lett 501:192–201

Allabar A, Dobson KJ, Bauer CC, Nowak M (2020) Vesicle shrinkage in hydrous phonolitic melt during cooling. Contrib Mineral Petrol. https://doi.org/10.1007/s00410-020-1658-3

Bagdassarov N, Dorman A, Dingwell DB (2000) Effect of alkalis, phosphorus, and water on the surface tension of haplogranite melt. Am Mineral 85:33–40

Barone G, Mazzoleni P, Corsaro RA, Costagliola P, Di Benedetto F, Ciliberto E, Gimeno D, Bongiorno C, Spinella C (2016) Nanoscale surface modification of Mt Etna volcanic ashes. Geochim Cosmochim Acta 174:70–84

Behrens H et al (1996) Near-infrared spectroscopic determination of water species in glasses of the system $MAlSi_3O_8$(M=Li, Na, K): an interlaboratory study. Chem Geol 128:41–63

Berndt J, Liebske C, Holtz F, Freise M, Nowak M, Ziegenbein D, Hurkuck W, Koepke J (2002) A combined rapid-quench and H_2-membrane setup for internally heated pressure vessels: Description and application for water solubility in basaltic melts. Am Mineral 87:1717–1726

Cahn JW (1965) Phase separation by spinodal decomposition in isotropic systems. J Chem Phys 42:93–99

Cahn JW, Hillard JE (1959) Free energy of a nonuniform system, III: nucleation in a two-component incompressible fluid. J Chem Phys 31:688–699

Cioni R (2000) Volatile content and degassing processes in the AD79 magma chamber at Vesuvius (Italy). Contrib Mineral Petrol 140:40–54

Cioni R, Civetta L, Marianelli P, Metrich N, Santagrone R, Sbrana A (1995) Compositional Layering and Syn-ruptive Mixing of a Periodically Refilled Shallow Magma Chamber: the AD79 Plinian Eruption of Vesuvius. J Petrol 36:739–776

Cormier L, Dargaud O, Calas G, Jousseaume C, Papin S, Trcera N, Cognigni A (2015) Zr environment and nucleation role in aluminosilicate glasses. Mater Chem Phys 152:41–47

Dargaud O, Cormier L, Menguy N, Patriarche G, Calas G (2011) Mesoscopic scale description of nucleation processes in glasses. Appl Phys Lett 99:021904

Debenedetti PG (2000) Phase separation by nucleation and by spinodal decomposition: fundamentals. In: Kiran E, Debenedetti PG, Peters CJ (eds.), Supercritical Fluids. In: Nato Science Series E, vol.366, pp 123–166

Devine JD, Gardner JE, Brack HP, Layne GD, Rutherford MJ (1995) Comparison of microanalytical methods for estimating H2O contents of silicic volcanic glasses. Am Mineral 80:319–328

Di Genova D, Sicola S, Romano C, Vona A, Fanara S, Spina L (2017a) Effect of iron and nanolites on Raman spectra of volcanic glasses: A reassessment of existing strategies to estimate the water content. Chem Geol 475:76–86

Di Genova D, Kolzenburg S, Wiesmaier S, Dallanave E, Neuville DR, Hess KU, Dingwell DB (2017b) A compositional tipping point governing the mobilization and eruption style of rhyolitic magma. Nature 552:235–238

Di Genova D, Caracciolo A, Kolzenburg S (2018) Measuring the degree of "nanolitization" of volcanic glasses: Understanding syn-eruptive processes recorded in melt inclusions. Lithos 318–319:209–218

Duan ZH, Zhang ZG (2006) Equation of state of the H_2O, CO_2, and H_2O-CO_2 systems up to 10 GPa and 2573.15 K: Molecular dynamics simulations with ab initio potential surface. Geochim Cosmochim Acta 70:2311–2324

Fabbrizio A, Carroll MR (2008) Experimental constraints on the differentiation process and pre-eruptive conditions in the magmatic system of Phlegraean Fields (Naples, Italy). J Volcanol Geoth Res 171(1–2):88–102

Fanara S, Botcharnikov RE, Husen A, Buddensieck J, Behrens H (2012) Pre-eruptive conditions of the Campanian Ignimbrite eruption: experimental constraints from phase equilibria and volatile solubility studies. In: Proceedings of IODP-ICDP Kolloquium, Kiel, Germany, 41–43.

Fanara S, Behrens H, Zhang YX (2013) Water diffusion in potassium-rich phonolitic and trachytic melts. Chem Geol 346:149–161

Foden J (1986) The petrology of Tambora volcano, Indonesia: a model for the 1815 eruption. J Volcanol Geotherm Res 27:1–41

Fortelný I, Živný A, Jůza J (1999) Coarsening of the phase structure in immiscible polymer blends. Coalescence or ostwald ripening? J Polym Sci 37:181–187

Gardner JE, Ketcham RA (2011) Bubble nucleation in rhyolite and dacite melts: temperature dependence of surface tension. Contrib Mineral Petrol 162:929–943

Gardner JE, Hilton M, Carroll MR (1999) Experimental constraints on degassing of magma: Isothermal bubble growth during continuous decompression from high pressure. Earth Planet Sci Lett 168:201–218

Genareau K, Proussevitch AA, Durant AJ, Mulukutla G, Sahagian DL (2012) Sizing up the bubbles that produce very fine ash during explosive volcanic eruptions. Geophys Res Lett 39:L15306

Gervasoni F, Klemme S, Rocha-Júnior ERV, Berndt J (2016) Zircon saturation in silicate melts: a new and improved model for aluminous and alkaline melts. Contrib Mineral Petrol 171:21

Giordano D, Russell JK, Dingwell DB (2008) Viscosity of magmatic liquids: A model. Earth Planet Sci Lett 271:123–134

Gonnermann HM, Manga M (2007) The fluid mechanics inside a volcano. Annu Rev Fluid Mech 39:321–356

Gurioli L, Houghton BF, Cashman KV, Cioni R (2005) Complex changes in eruption dynamics during the 79 AD eruption of Vesuvius. Bull Volcanol 67:144–159

Hajimirza S, Gonnermann HM, Gardner JE, Giachetti T (2019) Predicting homogeneous bubble nucleation in rhyolite. JGR Solid Earth 124:2395–2416

Hamada M, Laporte D, Cluzel N, Koga KT, Kawamoto T (2010) Simulating bubble number density of rhyolitic pumices from Plinian eruptions: constraints from fast decompression experiments. Bull Volcanol 72:735–746

Higgins MD (2000) Measurement of crystal size distributions. Am Mineral 85:1105–1116

Hurwitz S, Navon O (1994) Bubble nucleation in rhyolitic melts – experiments at high-pressure, temperature and water content. Earth Planet Sci Lett 122:267–280

Iacono-Marziano G, Schmidt BC, Dolfi D (2007) Equilibrium and disequilibrium degassing of a phonolitic melt (Vesuvius AD 79 "white pumice") simulated by decompression experiments. J Volcanol Geotherm Res 161:151–164

Kueppers U, Scheu B, Spieler O, Dingwell DB (2006) Fragmentation efficiency of explosive volcanic eruptions: a study of experimentally generated pyroclasts. J Volcanol Geotherm Res 153:125–135

Marxer H, Bellucci P, Nowak M (2015) Degassing of H_2O in a phonolitic melt: a closer look at decompression experiments. J Volcanol Geotherm Res 297:109–124

Mastrolorenzo G, Brachi L, Canzanella A (2001) Vesicularity of various types of pyroclastic deposits of Campi Flegrei volcanic field: evidence of analogies in magma rise and vesiculation mechanisms. J Volcanol Geotherm Res 109:41–53

Mcintosh I, Llewellin E, Humphreys M, Nichols A, Burgisser A, Schipper CI, Larsen J (2014) Distribution of dissolved water in magmatic glass records growth and resorption of bubbles. Earth Planet Sci Lett 401:1–11

Mourtada-Bonnefoi C, Laporte D (2004) Kinetics of bubble nucleation in a rhy-olitic melt: an experimental study of the effect of ascent rate. Earth Planet Sci Lett 218:521–537

Mujin M, Nakamura M (2014) A nanolite record of eruption style transition. Geology 42:611–614

Mujin M, Nakamura M, Miyake A (2017) Eruption style and crystal size distributions: crystallization of groundmass nanolites in the 2011 Shinmoedake eruption. Am Mineral 102(12):2367–2380

Nowak M, Behrens H (1997) An experimental investigation of diffusion of water in haplogranitic melts. Contrib Mineral Petrol 126:365–376

Nowak M, Behrens H (2001) Water in rhyolitic magmas: getting grip on a slippery problem. Earth Planet Sci Lett 184:515–522

Nowak M, Cichy SB, Botcharnikov RE, Walker N, Hurkuck W (2011) A new type of high-pressure low-flow metering valve for continuous decompression: first experimental results on degassing of rhyodacitic melts. Am Mineral 96:1373–1380

Ochs F, Lange R (1999) The density of hydrous magmatic liquids. Science 283:1314–1317

Preuss O, Marxer H, Ulmer S, Wolf J, Nowak M (2016) Degassing of hydrous trachytic Campi Flegrei and phonolitic Vesuvius melts: experimental limita-tions and chances to study homogeneous bubble nucleation. Am Mineral 101:859–875

Proussevitch AA, Sahagian DL (1996) Dynamics of coupled diffusive and decompressive bubble growth in magmatic systems. J Geophys Res 101:17,447–17,455

Scaillet B, Pichavant M, Cioni R (2008) Upward migration of Vesuvius magma chamber over the past 20,000 years. Nature 455:216–219

Schlinger CM, Smith RM (1986) Superparamagnetism in volcanic glasses of the KBS tuff: Transmission electron microscopy and magnetic behavior. Geophys Res Lett 13:729–732

Schlinger CM, Rosenbaum JG, Veblen DR (1988) Fe-oxide microcrystals in welded tuff from southern Nevada: Origin of remanence carriers by precipitation in volcanic glass. Geology 16:556–559

Schmidt BC, Behrens H (2008) Water solubility in phonolite melts: Influence of melt composition and temperature. Chem Geol 256:259–268

Sharp TG, Stevenson RJ, Dingwell DB (1996) Microlites and "nanolites" in rhyolitic glass: Microstructural and chemical characterization. Bull Volcanol 57:631–640

Shea T (2017) Bubble nucleation in magmas: a dominantly heterogeneous process? J Volcanol Geotherm Res 343:155–170

Shea T, Larsen JF, Gurioli L, Hammer JE, Houghton BF, Cioni R (2009) Leucite crystals: surviving witnesses of magmatic processes preceding the 79AD eruption at Vesuvius, Italy. Earth Planet Sci Lett 281(1–2):88–98

Shea T, Gurioli L, Larsen JF, Houghton BF, Hammer JE, Cashman KV (2010a) Linking experimental and natural vesicle textures in Vesuvius 79AD white pumice. J Volcanol Geotherm Res 192:69–84

Shea T, Houghton BF, Gurioli L, Cashman KV, Hammer JE, Hobden BJ (2010b) Textural studies of vesicles in volcanic rocks: An integrated methodology. J Volcanol Geotherm Res 190:273–289

Shea T, Gurioli L, Houghton BF (2012) Transitions between fall phases and pyroclastic density currents during the AD 79 eruption at Vesuvius: building a transient conduit model from the textural and volatile record. Bull Volcanol 74:2363–2381

Shea T, Hellebrand E, Gurioli L, Tuffen H (2014) Conduit- to Localized-scale Degassing during Plinian Eruptions: Insights from Major Element and Volatile (Cl and H$_2$O) Analyses within Vesuvius AD 79 Pumice. J Petrol 55:315–344

Sparks RSJ (1978) The dynamics of bubble formation and growth in magmas: a review and analysis. J Volcanol Geotherm Res 3:1–37

Tanaka H, Yokokawa T, Abe H, Hayashi T, Nishi T (1990) Transition from metastability to instability in a binary–liquid mixture. Phys Rev Lett 65:3136–3139

Toramaru A (2006) BND (bubble number density) decompression rate meter for explosive volcanic eruptions. J Volcanol Geotherm Res 154:303–316

Watson EB, Harrison TM (1983) Zircon saturation revisited: temperature and composition effects in a variety of crustal magma types. Earth Planet Sci Lett 64:295–304

Webster JD, Golfogg B, Stinoni MF, Shimizu N, De Vivo B (2014) C-O-H-Cl-S-F Volatile Solubilities, Partitioning, and Mixing in Phonolitic-Trachytic Melts and Aqueous-CarbonicVapor±Saline Liquid at 200MPa. J Petrol 55:2217–2248